Model-based Design of Low Frequency Lamb Wave EMATs for Mode Selectivity

Matthias Seher[1], Peter Huthwaite[1], Michael J. S. Lowe[1], Peter B. Nagy[1,2]
1 Department of Mechanical Engineering, Imperial College London, London, UK
2 Department of Aerospace Engineering and Engineering Mechanics,
University of Cincinnati, Cincinnati, Ohio, USA

Accepted for publication in Journal of Nondestructive Evaluation, June 2015
The final publication is available at Springer via http://dx.doi.org/10.1007/s10921-015-0296-6

Abstract

A low-frequency, omni-directional A0 Lamb wave ElectroMagnetic Acoustic Transducer (EMAT) is developed for applications in guided wave tomography, operating at 50 kHz on a 10 mm thick steel plate. The key objective is to excite an acceptably pure A0 wave mode in relation to the S0 mode, which can also be present at this operating point and is desired to be suppressed by approximately 30 dB. For that, a parametric Finite Element (FE) model of the design concept is implemented in a commercially available FE software, where the bias magnetic field is calculated initially, then combined with the eddy current caused by the induction coil to produce a force. A numerical optimization process employing a genetic algorithm is set up and the EMAT design is optimized to yield an improved A0 mode selectivity. The parameters subjected to optimization are the magnet diameter and the magnet lift-off, which control the direction of the exciting force in the skin depth layer and therefore the mode selectivity. Although there are three possible electromagnetic acoustic interaction mechanisms, the optimisation considers only the Lorentz force, as its performance surface contains a clear optimum and from the optimised design a physical prototype is built. The FE model is validated against measurements on an aluminium plate for the Lorentz force excitation mechanism and on a steel plate for both the Lorentz and magnetisation force. For the steel plate, it is found that only considering the Lorentz force leads to a significant overestimation of the mode selectivity, as the S0 amplitude is underestimated by the Lorentz force, but the A0 amplitude remains mainly uninfluenced. Further, it has been found that additionally including the magnetisation force into the optimisation leads to a better mode selectivity, however, the optimisation drives the optimum to a minimum magnet diameter and therefore reduces the EMAT sensitivity. In a numerical study robustness is shown for fairly large variations of the magnet lift-off and the magnetic permeability. Based on the findings, a two-step model-based design approach is proposed whereby only the Lorentz force is used in the first step for the optimisation and then in a second step, a realistic estimate of the mode selectivity of the optimised design can be obtained by additionally considering the magnetisation force.

1 Introduction

Detecting and characterising corrosion type defects on pipelines is one of the major inspection problems faced by the petrochemical industry and is especially challenging in regions of interest with restricted access. One approach for the measurement of the remaining wall thickness is guided wave tomography, where the dispersive nature of guided waves is exploited to reconstruct a thickness map of the region of interest based on known dispersion relations. A challenging aspect of guided wave tomography is that multiple Lamb wave modes can exist at any one frequency, even at low frequencies. One strategy is to simply send and receive multiple

modes [1, 2], however, the thickness reconstruction may suffer due to uncertainties in the signal processing. By comparison, attempts to excite and measure a single Lamb wave mode by careful transduction have shown superior results, using the S0 mode in [3–5] and the A0 mode in [6, 7], allowing for highly accurate thickness maps of complex defects to be produced. The relative merits of the A0 and S0 mode are discussed in [8] and based on this, here the focus is on exploiting A0 waves, which have been shown to be more sensitive than S0 to the majority of corrosion defects.

One of the practical issues identified in [9] is the array scattering from the piezoelectric A0 Lamb wave transducers bonded to a plate, which correspond to a localised thickness change and interferes with the ability to attribute the scattered wave field to the defect by the imaging algorithm. Physically this means that the scattering from the transducers generates (coherent) noise that masks the scattering from the defect and thus negatively influences the thickness reconstruction. This problem of transducer array scattering can be overcome by utilising contactless transduction, which can be achieved with, for example, electromagnetic acoustic transducers (EMATs) [10]. While EMATs can suffer from a low signal-to-noise ratio and can only excite elastic waves in conducting materials, for guided wave tomography applications the ability to avoid transducer scattering prevails and makes them invaluable. Therefore, the focus here is extended to developing a selective A0 EMAT.

An EMAT consists of two main components, an induction coil and a permanent magnet, that are arranged so as to excite the desired wave type. For the generation of low frequency omni-directional A0 Lamb waves, a design is illustrated in Figure 1. Note that this design can also be adapted to excite S0 Lamb waves by changing the geometrical parameters [11]. In Figure 1, a pancake coil is placed above the specimen surface and is driven by an alternating current, inducing eddy currents in a skin depth layer within the specimen. The permanent magnet is located coaxially above the specimen and the pancake coil and provides a bias magnetic field that penetrates the specimen. The interaction of the dynamic magnetic field of the eddy currents and the bias magnetic field of the permanent magnet produces a force, which gives rise to elastic waves in the specimen. In reception, the elastic wave generates an electromotive force that induces a voltage in the induction coil of the receiving EMAT and can be measured at the terminals of the coil.

When developing an EMAT based on the design concept of Figure 1, a set of requirements need to be fulfilled in order for the EMAT to be useful for A0 Lamb wave tomography. Firstly, the operation point for the EMAT is given by the operation point of the tomography system and is chosen here to be at a frequency of 50 kHz on a 10 mm thick plate. This is illustrated in Figure 2, where the dispersion curves for the lower order Lamb modes in a steel plate are shown; the reasons for this operation point are discussed in [8]. Also, as seen from Figure 2, at the designated operation point, there are two modes present, the A0 and the S0 mode. The S0 mode exhibits a much greater group velocity, which implies that any excited S0 waveform will arrive before the A0 waveform. Since any scattered and reflected components of a wave typically arrive after the main wave packet, this means that these components of the S0 waves may corrupt the main A0 signal. For that reason, a target S0 suppression of approximately 30 dB in relation to the A0 mode, measured for an EMAT to EMAT send-receive setup, is required, as this will push the S0 amplitude to the order of the noise of a typical EMAT system. Lastly, the EMAT is required to work on steel, which is a ferromagnetic material and therefore requires additional consideration in the development.

The goal of this paper is to develop and implement a physical prototype of an omni-directional, low frequency, A0 Lamb wave EMAT, based on the design in Figure 1 and the requirements given above. One aspect that needs to be considered in the development is the duality of mode selectivity and sensitivity (signal-to-noise ratio). While the mode selectivity is given by how purely the EMAT excites the A0 over the S0 mode, the sensitivity regards how well either can be detected relative to the noise. Here, mode selectivity prevails over sensitivity

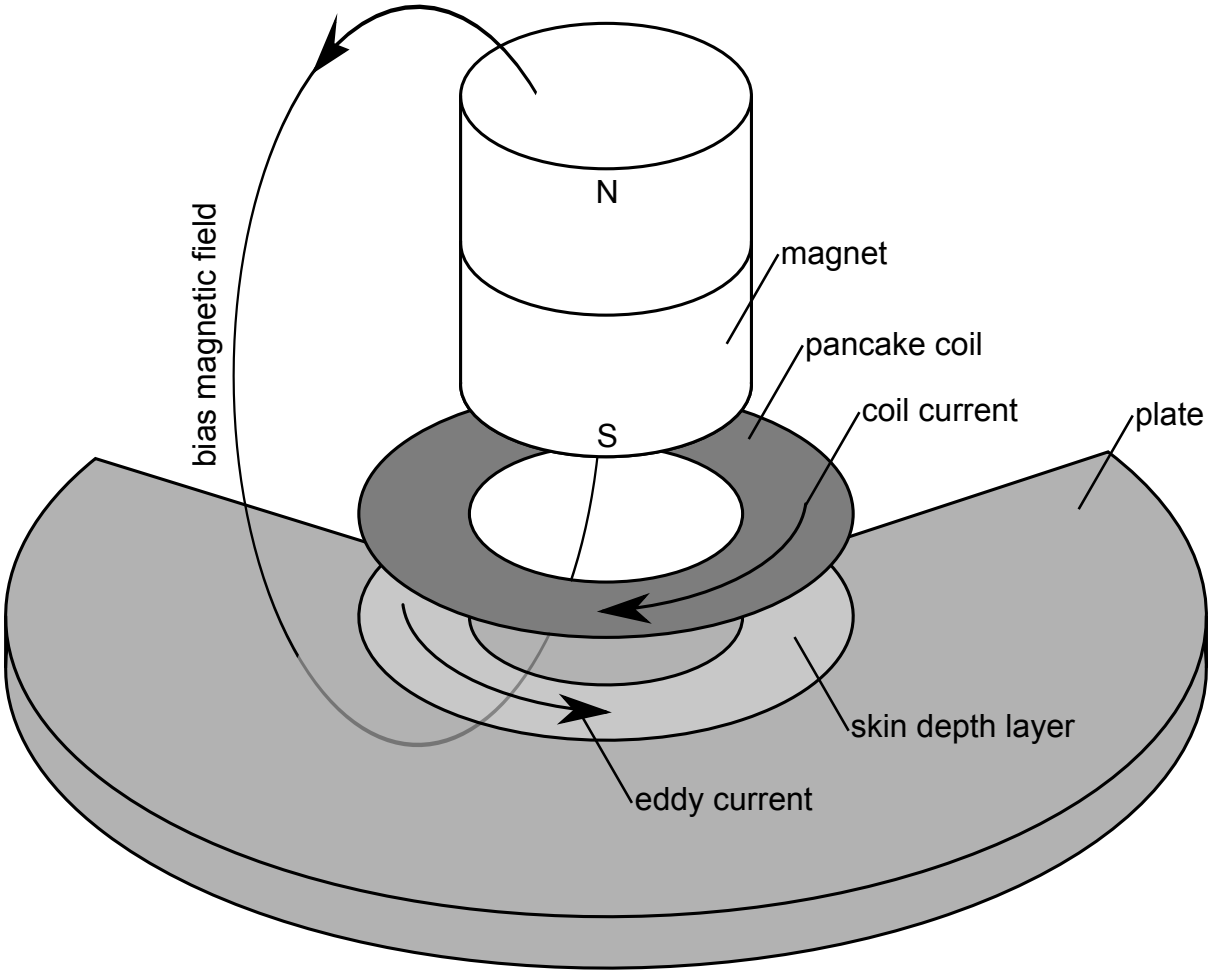

Figure 1: Design concept of an omni-directional, low frequency, Lamb wave EMAT, showing the permanent magnet and the induction coil. The skin depth layer and the direction of the magnetic field and the coil and induced eddy current are illustrated.

and potential sensitivity issues may be overcome with more powerful measurement electronics. The sensitivity may be additionally enhanced by tuning, for example, the coil geometry or the coil impedance, which is a topic of ongoing research, or by specialised magnetic flux shaping to increase the magnetic flux density in the eddy current layer (such as in [12]).

A parametric numerical Finite Element (FE) model based on the design concept from Figure 1 is developed, in order to meet the design requirements. An optimisation procedure using a genetic algorithm is applied to the FE model to enhance the mode selectivity with the aim to improve the EMAT design until the necessary S0 suppression requirement is met. In the following, first the theoretical background is presented, followed by the overview of the employed numerical model and optimization. In the results section, first the simulation results for the optimised design are presented. An experimental prototype is built from this design and the model is validated on an aluminium and a steel plate. Further, various aspects concerning the optimisation and robustness of the design are discussed and a model-based design approach is proposed, which represents the main novelty of this paper.

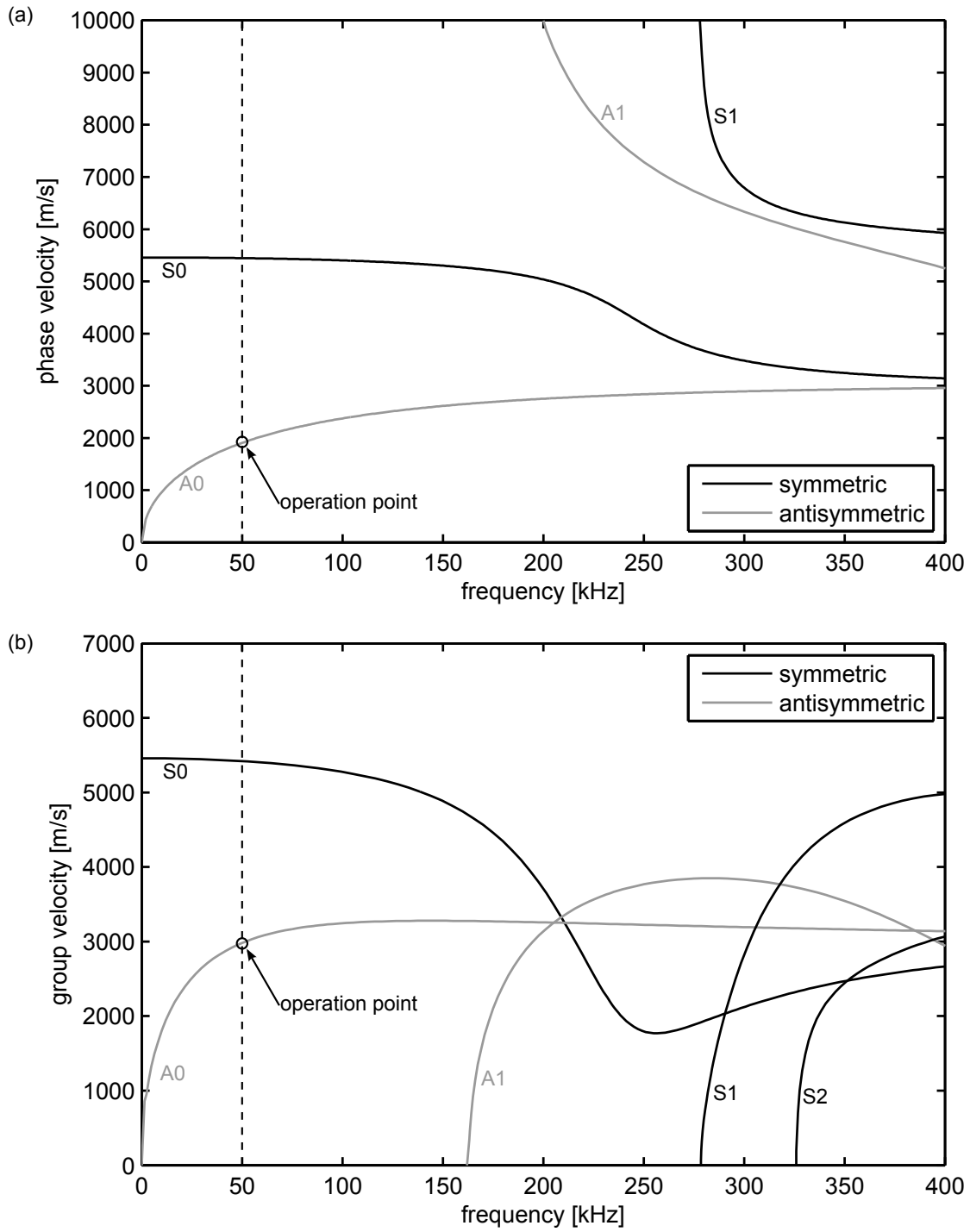

Figure 2: Dispersion curves for the lower order Lamb modes in a 10 mm thick steel plate, illustrating the phase velocity (a) and the group velocity (b). The dispersion curves are computed with DISPERSE [13].

2 Theoretical Background

2.1 Electromagnetic Acoustic Coupling

In the field of electromagnetic acoustic transduction, electromagnetic and elastodynamic domains are coupled to produce stress waves from the changes of the electromagnetic field quanti-

ties. In the following, the derivations are based on [14–16] and represent a brief overview of the mathematical treatment of the electromagnetic acoustic coupling. The variables in bold font denote vector/tensor quantities, whereas regular fonts represent scalar quantities.

In the scope of this research, the magneto-quasi-static approximation of the Galilean limit [17] of Maxwell's equations can be employed. The solution to Maxwell's equations yields a propagating wave solution when solved for any frequency, which is caused by the time derivative of the electric flux density added by Maxwell to Ampère's law. However, for frequencies below 100 MHz and in good conductors [14], this term may be omitted from Maxwell's equations, which then represent a set of parabolic partial differential equations, an example of which is the diffusion equation. In [14] it is shown that in good conductors the free charge density decays to zero virtually instantly (exponentially with an electric charge diffusion time on the order of $\tau \approx 10^{-20}\,\mathrm{s}$, for example, for steel), due to the high electric conductivity σ ($\tau \propto 1/\sigma$) values of the respective material. Therefore, it can be assumed for our modelling purposes that any change in the electromagnetic field quantities occurs instantaneously throughout the regarded spatial domain.

The simplification of neglecting Maxwell's correction to Ampère's law mathematically expresses the skin effect as one of the implications of the diffusion equation. The skin effect describes the exponential decay of the electromagnetic quantities due to an alternating electromagnetic field at the surface. The skin depth is defined as in [14] as

$$\delta = \sqrt{\frac{1}{\pi f \sigma \mu}}. \tag{1}$$

Equation (1) calculates the skin depth δ for a material with conductivity σ and magnetic permeability μ impinged upon by an electromagnetic field at a frequency of f.

With the above assumptions, Maxwell's equations may be given in terms of the magnetic vector potential $\mathbf{A}$, such that

$$\nabla^2 \mathbf{A} - \mu\sigma \frac{\partial \mathbf{A}}{\partial t} = -\mu \mathbf{J_e}. \tag{2}$$

In equation (2), $\mathbf{J_e}$ represents the externally applied current density. From the magnetic vector potential, the magnetic flux density ($\mathbf{B} = \nabla \times \mathbf{A}$) and electric field $\mathbf{E} = -\dot{\mathbf{A}}$ may be computed. The induced current density can be given as $\mathbf{J} = -\sigma \dot{\mathbf{A}}$ using Ohm's law. In addition to equation (2), for the computation of electromagnetic fields, a gauging condition is introduced, such as the Coulomb gauge ($\nabla \cdot \mathbf{A} = 0$).

The solution to Maxwell's equation in any representation requires a set of constitutive relationships interrelating the various electromagnetic field variables. The constitutive relationships depend on the material properties of the electromagnetic continuum and are generally nonlinear. For ferromagnetic materials the magnetic flux density $\mathbf{B}$ can be expressed as a function of the magnetizing field $\mathbf{H}$ such that $\mathbf{B} = \mu(\mathbf{H})\,\mathbf{H}$, assuming an isotropic behaviour. In this paper, this constitutive relationship is assumed to be linear, for simplicity and due to its high uncertainty, such that $\mathbf{B} = \mu_0 \mu_r \,\mathbf{H}$, with $\mu_0 = 4\pi \times 10^{-7}\,\mathrm{Vs/Am}$ being the permeability of vacuum and μ_r the relative permeability. Another representation of this reads $\mathbf{B} = \mu_0(\mathbf{H} + \mathbf{M})$, where $\mathbf{M}$ denotes the magnetization in the material.

The interaction of electromagnetic fields with conducting elastic domains gives rise to elastic deformations. The elastic deformations cause changes in the electromagnetic field quantities, making coupling generally bidirectional. However, for EMAT applications, hierarchical coupling can be assumed [18], as the changes in the electromagnetic quantities due to elastodynamic phenomena are small and so can be neglected. This enables the separation of both domains and in a first step the electromagnetic phenomena can be computed and then the results can be utilized for the determination of the elastic domain excitation. The coupling of the electromagnetic and elastic domain is determined by three major mechanisms [14, 19].

The first mechanism is the Lorentz force, which describes the forces acting on static and moving charges. However, as the magneto-quasi-static approximation is considered, the net

charge density is zero due to the short electric charge diffusion time τ and therefore can be neglected in the force calculation, so that the Lorentz body force becomes

$$\mathbf{f}^L = \mathbf{J} \times \mathbf{B}. \tag{3}$$

The second interaction mechanism between the electromagnetic and elastic domains is the magnetization force [20, 21]. The magnetization force can be understood as the forces acting on magnetic dipole moments in the presence of a (spatially varying) magnetic field. The total magnetization force can be calculated as

$$\mathbf{F}^{mag} = \mu_0(\mu_r - 1) \int_V (\mathbf{H} \cdot \nabla)\mathbf{H} \, \mathrm{d}V + \frac{(\mu_r - 1)^2}{2\mu_0 \mu_r^2} \int_S B_n^2 \mathbf{n} \, \mathrm{d}S. \tag{4}$$

Equation (4) describes the total magnetisation force acting on the body given as a function of the total magnetising field $\mathbf{H}$ and magnetic flux density $\mathbf{B}$. It is composed of two terms, a volume integral, which relates to the forces in the body due to external and internal sources and a surface integral over the surface of the whole body, which is required due to the discontinuity of the relative magnetic permeability at a material interface. In equation (4), the surface integral is expressed in terms of the magnetic flux density to facilitate the computation, as the normal component of the magnetic flux density is continuous across a material interface. This formulation of the magnetisation force assumes a paramagnetic constitutive relationship as an approximation for a ferromagnetic constitutive relationship and the authors acknowledge that this may be an oversimplification. One implication of this is that no magnetic saturation occurs in the body and it needs to be ensured that this condition is met. Further, in equation (4), ∇ denotes the Nabla or del vector operator and the term in parentheses condenses to a scalar operator due to the dot product between the magnetization $\mathbf{H}$ and the Nabla operator.

The third interaction mechanism is magnetostriction and represents a constitutive relationship between the strain and the magnetizing field. Magnetostriction is neglected in this paper, as it exhibits vast uncertainties in the material parameters and it is expected that for the EMAT design here would only have a small influence, in accordance with the findings in [22].

The governing equations for the elastodynamic domain are obtained from the localized version of the balance of linear momentum [23] (page 500). By assuming a linear isotropic elastic constitutive relationship between the Cauchy stress tensor and the elastic strain tensor, such as Hook's law, the equation of motion of the linear elastic domain reads

$$(\lambda' + \mu')\nabla(\nabla \cdot \mathbf{u}) + \mu' \nabla^2 \mathbf{u} - \rho \frac{\partial^2 \mathbf{u}}{\partial t^2} = -\rho \mathbf{f}. \tag{5}$$

Equation (5) is also known as Navier's equation of motion and λ' and μ' represent the Lamé constants; ρ denotes the mass density and $\mathbf{u}$ the particle displacement, and the variable $\mathbf{f}$ denotes the body force acting on the regarded elastic continuum. When only considering the Lorentz force as an excitation mechanism, equation (3) can be substituted directly for $\mathbf{f}$. In the case where the magnetisation force is considered, equation (4) needs to be adapted slightly, such that the localised version of the volume integral is substituted for the body force $\mathbf{f}$ and the surface integral term represents a traction boundary condition. The body force (with traction boundary condition in case of the magnetisation force) is also the coupling term for a weak coupling between the electrodynamic and the elastodynamic domains.

2.2 Lamb Waves

Figure 2 shows the dispersion curves for the lower order Lamb modes and it can be seen that at the designated operation point, two Lamb modes exist, S0 and A0. The goal of this paper is to preferentially suppress the S0 mode over the A0 mode and because of this, the respective mode shape of each mode must be considered so that the exciting forces generate the A0 mode

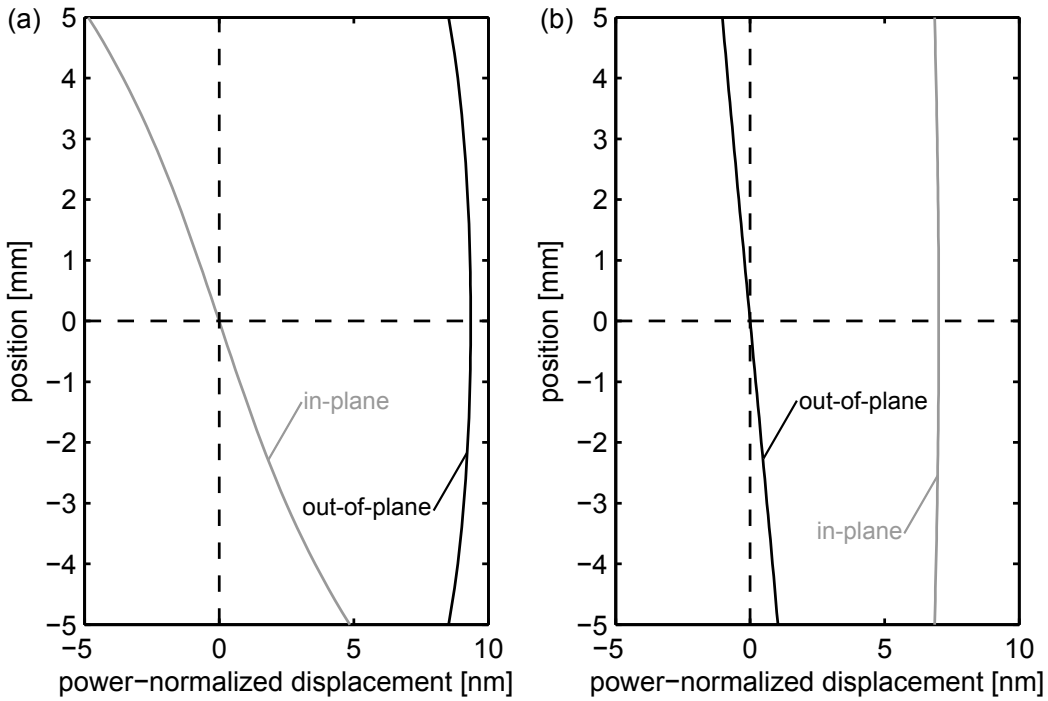

Figure 3: In-plane and out-of-plane displacements for a unit power flow for the A0 mode (a) and the S0 mode (b) across the thickness direction of the plate (origin at mid-thickness), shown for an operation point at 50 kHz on a 10 mm thick steel plate (using typical values for material parameters).

as purely as possible. In Figure 3, the power-normalized mode shapes (in-plane and respective out-of-plane displacements) for the A0 and S0 modes are depicted as a function of the thickness coordinate in the plate for the desired operation point. The power-normalization ensures that the waves have a unit power flow in the direction of propagation and is chosen to enable a direct comparison between the two modes shapes. For the A0 mode, which is pictured in Figure 3(a), the out-of-plane displacement clearly outweighs the in-plane displacement. On the other hand, for the S0 mode, which is displayed in Figure 3(b), the in-plane displacement is greater than the out-of-plane displacement. In EMAT applications, non-negligible forces only occur in the skin depth layer, which has a frequency dependent thickness given by (1) and is approximately $\delta = 67\,\mu$m at the designated operation point. This means that for the excitation of a particular Lamb mode, the body forces within the skin depth layer (and additionally the surface traction in case of the magnetisation force) control the mode selectivity. By decomposing the applied forces into their in-plane and out-of-plane components, the contributions of each component to the various modes can be computed. This approach has been presented in [24] for the excitation of Lamb waves due to a point force excitation. Wilcox et al. [11] extended these findings to their analytical model of an S0 Lamb wave EMAT operating on aluminium plates. This approach gives rise to the concept of force shaping, in order to excite a specific Lamb mode. The idea of force shaping is to approximate the ratio of the in-plane and out-of-plane displacements near the surface of the plate with a respective body force distribution, typically over a distance of half the wavelength. A second type of force shaping exploits the Poisson effect, whereby the in-plane and out-of-plane components of the excitation force are balanced such that the unwanted mode is suppressed. The concept of force shaping is applied in the model-based design approach.

3 Model Overview and Optimization

In this section, an overview of the EMAT model including the various physics and modelling aspects is given, followed by the introduction of the numerical optimization process and the development of an optimization criterion.

3.1 Model Overview

Figure 4(a) shows the layout of the model of the EMAT and represents a cross-section through a symmetry plane of Figure 1. The global coordinate reference frame for the model is placed on the upper surface of the plate, as shown in Figure 4(a). By exploiting the axisymmetric nature of the EMAT design, a cylindrical coordinate system can be assumed, where the axial direction (z-axis) coincides with the cylinder axis of the permanent magnet. The radial coordinate axis (r-axis) then is parallel to the surface of the plate. Clearly this axisymmetric model will be unable to represent a domain containing both the transmitting and receiving transducer and will therefore only be used to estimate the performance of the design in transmission. However, the relative sensitivities to A0 and S0 in reception will be the same as the relative sensitivities when transmitting, provided the values have been power-normalised. The cable-to-cable A0-S0 ratio can therefore be computed by squaring the power-normalised A0-S0 ratio from the transmission case.

Figure 4(a) also shows the geometric parameters of the model. Apart from the magnet diameter (d_magnet) and the magnet lift-off from the top of the coil (s_liftoff), which are subjected to optimization, all other parameters are maintained constant at the illustrated values. The inner and outer diameters of the induction coil are taken from [11], where they match the values for the coil of EMAT VII. It was shown in [11] that mode selectivity can be controlled by the coil dimensions, such that if the average diameter of the induction coil is approximately half the wavelength of the desired Lamb mode, then the excitation of that mode is maximized.

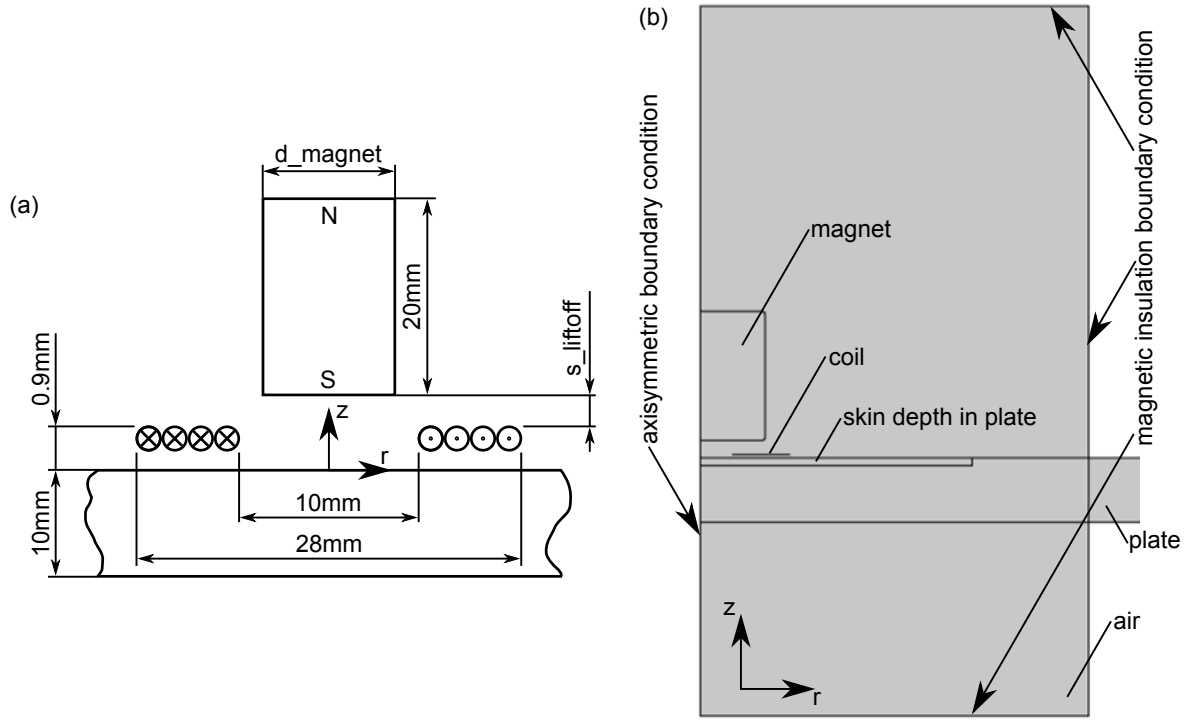

Figure 4: Overview of the EMAT model and the various geometric parameters used (a). In (b) the implementation in COMSOL is illustrated.

This is the case here, where for the operation point of 50 kHz on a 10 mm thick steel plate, the A0 wavelength is 37 mm, which is approximately twice the average coil diameter of 19 mm. In contrast, the wavelength of the S0 mode is approximately 107 mm at the same operation point and this vast difference in wavelength may significantly contribute to the mode selectivity of the transducer. The number of turns of the induction coil is not included as an optimisation parameter, as it was shown in [11] that this parameter only increases the sensitivity of the EMAT with increasing number of turns. Ongoing research suggests that in the light of signal-to-noise ratio computations, the number of turns may be a parameter that can be tuned to enhance the EMAT sensitivity in correlation with the measuring electronics.

The model is numerically implemented using the FE software COMSOL [25] to model and simulate the EMAT under development. The modelling approach employed is adapted from [26], where the software COMSOL was used to model and simulate EMATs for shear wave applications. In [26], this model is experimentally validated and, given the similarity to the model proposed here, a realistic behaviour of the model is expected. In contrast to the work in [26], this paper additionally implements the bias magnetic field within the model, so that the geometric parameters of the magnet may participate in controlling the mode selectivity between the A0 and S0 modes.

Figure 4(b) depicts the EMAT model as it is implemented in COMSOL. In addition to Figure 4(a), an air domain is added that engulfs the magnet and the induction coil. The air domain is necessary in order to model the return path of the magnetic flux from the permanent magnet and induction coil outside the steel plate. It should behave as if it is of infinite extent; therefore it is set sufficiently large (60 mm in radial and 110 mm in axial direction) such that the magnetic insulating boundary conditions can be assumed to have a negligible effect on the model across the full range of design parameters. Further, the air domain is only associated with the electromagnetic physics and so is localized to the transducer part of the model, but is omitted for the plate elsewhere. The omission of the air domain is a common assumption for elastic wave propagation in solids, as the difference in mechanical impedance at the air-to-solid interface is large enough and it can be assumed that no energy is lost to the air domain. This approach also helps to reduce the computational effort, as the elastic wave field does not need to be computed in the air domain. The edge of the plate, which extends 1.2 m in the radial direction, is terminated with Perfectly Matched Layers (PMLs) [25], in order to emulate an infinite extent in the radial direction and avoid end reflections. The application of PML regions is necessary, as the COMSOL simulations are conducted in the frequency domain and therefore edge reflections cannot be avoided by gating off the reflected waves from the time traces, unlike for time domain simulations.

The computation of the bias magnetic field generated by the permanent magnet requires the material parameters to be defined. The electromagnetic parameters for the various materials involved are listed in Table 1. The permanent magnet is modelled as a N42 grade Neodymium-Iron-Boron magnet (material parameters taken from [27]). The constitutive relationship between the magnetizing field $\mathbf{H}$ and the magnetic flux density $\mathbf{B}$ is assumed to be $\mathbf{B} = \mu_0\mu_r\mathbf{H} + \mathbf{B_r}$, where $\mathbf{B_r}$ is the remnant magnetic flux density vector and takes a value of $|\mathbf{B_r}|$=1.3 T in case of a N42 grade magnet. The orientation of the remnant flux density points in the positive z-direction, as within the magnet the magnetic flux lines run from the south to the north pole. Further, for the effective relative magnetic permeability of the magnet, the recoil permeability is assumed. The air domain assumes a linear constitutive relationship and the electric conductivity of the air domain is given a very small, non-zero value in order to improve the numerical stability of the COMSOL solver as suggested in [25]. The electromagnetic constitutive relationship for the steel plate is also assumed to be linear, with a relative magnetic permeability of $\mu_r = 160$ [22]. It has been verified that across all possible design parameters there is no magnetic saturation in the steel plate, as this would violate the strong paramagnetic assumption, which is underlying to the magnetisation force computation. The relative electric

Table 1: Electromagnetic material parameters employed in the FE model.

Material	rel. permittivity ϵ_r	rel. permeability μ_r	el. conductivity σ
Air	1	1	10 S/m
N42 magnet	1	1.05	8×10^5 S/m
Steel	1	160	4.032×10^6 S/m

permittivity ϵ_r for all materials in Table 1 is selected as unity because these materials do not exhibit any sort of dielectric behaviour in EMAT applications.

The induction coil, which produces the dynamic magnetic field and induces the eddy currents in the steel plate, is modelled as a surface current. The value for the surface current density K is calculated from the number of turns of the coil N, the coil dimensions illustrated in Figure 4(a) and the electric current I in the wires such that

$$K = \frac{N}{l} I. \tag{6}$$

In equation (6), the variable l represents the coil length, which is given by the difference of the outer and inner coil radius. The factor N/l can be regarded as a coil parameter, as it gives the number of turns per unit length of the coil, assuming constant wire spacing. The coil modelled in this paper, which is taken from the coil of EMAT VII in [11], has 46 turns in two layers on a printed circuit board (PCB), leading to a factor of N/l=2.55 1/mm. For the simulations, the coil current I is set to 1 A and the model is solved in the frequency domain. For the dynamic magnetic field, the same mesh is used as for the bias magnetic field simulation.

The boundary conditions for the electromagnetic model are illustrated in Figure 4(b) and a magnetically insulating boundary condition ($\mathbf{n} \cdot \mathbf{B} = 0$) is assumed for the edges of the air domain, including the edge of the steel plate. The axis of symmetry is also modelled with a magnetically insulating boundary condition (symmetry boundary condition). The discretization of all domains of the FE model is achieved using quadratic triangular elements. The region of interest in the FE model is the skin depth layer, as illustrated in Figure 4(b) and represents the coupling region between the electromagnetic and elastodynamic physics. In this region the mesh density is extremely high, in order to correctly approximate the electromagnetic-elastodynamic interaction. A convergence study on a single wire over a half space FE model using COMSOL has been conducted in [26] by comparing the numerical results to an analytical solution given in [28]. It is found that at least one element per length of skin depth is necessary for accurate approximation. Due to the fact that the skin depth decreases with increasing frequency, the element size is determined by the maximum occurring frequency.

The elastic material properties of the plate are selected to be those of steel with a mass density ρ=7850 kg/m^3, Young's modulus E_{Young}=200 GPa and Poisson's ratio $\nu = 0.33$ for the elastodynamic simulation. The radius of the plate is chosen as 1.2 m, allowing the complete separation in the time domain of the S0 and A0 Lamb wave modes for a five cycle Hann-windowed tone burst centred at 50 kHz, when measured on the top surface of the plate. The centre line of the EMAT model (z-axis in Figure 4(a)) is the axis of axisymmetry and thus by definition the nodes on this line are fixed in the radial displacement. For the other three sides of the plate, traction-free surface boundary conditions are implemented (with the exception where the surface traction of the magnetisation force acts). The plate domain is discretized with quadratic triangular elements and the maximum element size is 1 mm, which corresponds to less than 1/30 of the wavelength for the A0 mode at 50 kHz. The accuracy of the elastodynamic physics at this discretization level is verified by comparing the phase velocity to the results from DISPERSE [13] and a discrepancy of less than 1% is found, rendering the discretization fine enough.

The time domain data for the evaluation of the simulation results is recovered using the method of Fourier synthesis, since all calculations with the exception of the bias magnetic field

are conducted in the frequency domain. The idea of Fourier synthesis is to use the frequency domain dataset that is computed by COMSOL to calculate the desired signal at all frequencies, then perform an inverse Fourier transform to obtain the time domain signal. The frequency dataset computed from the FE model is band limited to reduce the number of frequency evaluation points and hence the computation time. However, it is to be remarked that besides the band limits, the sampling rate and the length of the zero-padded input waveform also determine the number of frequency evaluation points. Suitable band limits can be established from the Fourier transform of the input toneburst; for the five-cycle Hann-windowed toneburst used in this paper it was found sufficient to include only frequencies within the main and first side lobes of the amplitude spectrum. The effect of this filtering can be validated by performing an inverse Fourier transform. For a centre frequency of 50 kHz this corresponds to a frequency band of 20 kHz to 80 kHz.

The electromagnetic simulation results of the bias magnetic field simulation and dynamic magnetic field simulation are used in a third step to compute the Lorentz body force, using equation (3) and the magnetization force, using equation (4), which act on the steel plate in the elastodynamic physics within the skin depth layer. The force calculation of the Lorentz force utilises the current density given by the simulation of the dynamic magnetic field of the induction coil and the magnetic flux density given by the simulation of the static magnetic field of the permanent magnet. The magnetisation force expressed by equation (4) describes the total force acting on the steel plate and is implemented in the FE model as a body force given by the argument of the volume integral, as well as a surface traction given by the argument of the surface integral. The traction force acts on the top surface of the skin depth region of Figure 4(b). For the computation of the body and traction forces, the electromagnetic field quantities are assumed to be the sum of the static and dynamic simulations and only the terms that yield contributions at the regarded frequency are considered. Further, it is assumed that the magnetisation force deforms the steel plate and is countered by a rigid permanent magnet that is fixed to the inertial frame.

3.2 Optimization Overview

The optimization process aims to improve the mode selectivity of the A0 mode over the S0 mode at the desired operation point. The mode selectivity here is controlled by the magnet diameter and the magnet lift-off, which determine the spatial variation of the bias magnetic field and therefore the force distribution in the skin depth layer and further the wave excitation.

The influence of the direction of the exciting forces on the mode selectivity is discussed by Nagy et al. in [29] for a simplified case, in order to better illustrate the concept of S0 suppression. For the derivations in [29], only the Lorentz force is considered, which is modelled via a traction cone. The whole magnetic effect is not modelled and disregarded for the discussion, as the emphasis is on the mode selectivity. One of the conclusions is that for certain angles between the traction force and the surface normal of the specimen, there exists a clear maximum in the A0-S0 ratio due to reduced excitation of the S0 mode, which is explained by the Poisson effect. Further, time traces from two different EMAT designs, one without and one with optimised traction forces, are presented and used to experimentally demonstrate the feasibility of the mode selectivity enhancement. For the design regarded here, it is expected that there should similarly be an optimum and that this should be found by the numerical optimization process. Additionally to [29], here the influence of the magnetic permeability is considered and for the wave excitation, a body force (and a surface traction in case of the magnetisation force) is assumed.

The optimization process requires a measure for the performance or fitness of every candidate design. The idea for the performance evaluation in this research is to relate the amplitude of the transmitted A0 Lamb mode to that of the S0 Lamb mode. Here, the performance metric γ is introduced and represents the ratio of the amplitudes of the A0 and S0 modes expressed in

[dB]:

$$\gamma = 20 \log_{10} \left(\alpha \frac{A_0}{S_0} \right)^2 . \tag{7}$$

Equation (7) describes the cable-to-cable A0-S0 ratio and the A0 and S0 amplitudes are determined by exploiting the different symmetries of the mode shapes on the neutral line of the plate (at mid thickness); the A0 amplitude there corresponds to the out-of-plane displacement (z-axis), whereas the S0 amplitude to the in-plane displacement (r-axis). The power-normalisation coefficient α takes a value of $\alpha = 0.752$ at the operation point of 0.5 MHz-mm on the steel plate and is determined at mid thickness. The evaluation of γ over the range of the radial coordinate has shown that for large enough distances away from the origin of the reference frame (in the far field), the performance index reaches a steady value, which is then used for the computations. All computations are carried out in the frequency domain at the operation frequency and it needs to be noted here that γ neglects the (absolute) mode sensitivity.

The optimization problem in this paper uses the genetic algorithm of [30], as it requires no prior knowledge of the behaviour of the performance function (here, no knowledge of the A0-S0 ratio as a function of the magnet diameter and lift-off) within the feasible design space and covers large areas of the feasible design space. Further, in contrast to gradient based methods, the genetic algorithm is less susceptible to converge to a local minimum. A practical advantage of the genetic algorithm is that it is already implemented in the Matlab Optimization Toolbox [31].

4 Results

In this section, first the optimisation results are presented and then the FE model is experimentally validated based on a physical prototype of the enhanced design. The major focus in this section is on the comparison between numerical simulations and experiment. Further, a numerical robustness study is conducted regarding two key parameters and a model-based design approach is presented.

4.1 Optimisation Results

The software implementation of the genetic algorithm for the optimization process uses the Matlab Optimization Toolbox [31] and a custom fitness function that conducts an FE simulation for every call, returning the respective performance index (see previous section). The optimization is conducted using a population of ten individuals and simulating ten generations, yielding a total of 110 function evaluations, as the initial population (zeroth generation) also needs to be evaluated. However, the optimal design is usually found after approximately five or six generations. The optimization is run on a workstation with two Intel(R) Xeon(R) CPU X5690 at 3.47 GHz with 6 cores and is completed in approximately two hours (for 110 performance function evaluations).

Table 2: Optimization results at 50 kHz on a steel plate based on the excitation with only the Lorentz force for the optimal design and proposed realisation. The cable-to-cable A0-S0 ratio for the case of both the Lorentz and magnetisation force are calculated based on the given magnet diameter and lift-off.

optimisation result	magnet diameter	magnet lift-off	cable-to-cable A0-S0 ratio	
			fLor	fLor+FMag
optimal design	21.05 mm	1.47 mm	83.6 dB	27.3 dB
proposed realization	20.0 mm	2.1 mm	82.1 dB	29.5 dB

The two design parameters subjected to optimization are bounded to confine the feasible design space to a smaller region and the bounds are set to a practical range: 5 mm to 30 mm for the magnet diameter and 1 mm to 3 mm for the magnet lift-off. At first, only the Lorentz force is considered as an excitation mechanism as it is well characterised and can be reliably calculated. The magnetisation force requires multiple assumptions about the ferromagnetic material properties and this exhibits a large degree of uncertainty. However, it is expected that the magnetisation force will influence the mode selectivity. Also, by only employing the Lorentz force, it is expected that some of the findings from [29] regarding mode selectivity could be recreated for the case of an extended coil, rather than the "single turn coil" regarded by Nagy et al.

The optimisation is run ten times to ensure convergence and it is found that the optimisation converges to the same region for all optimisation runs, implying a global minimum. From the optimization runs it is observed that multiple combinations of magnet diameter and lift-off yield similar performances of better than 75 dB for the A0-S0 ratio within this region. These optima maintain a high A0-S0 ratio for a large variation of the magnet lift-off, while the magnet diameter shows only slight variations. This implies that the magnet diameter is the dominant design parameter in the optimization and the gradient of the A0-S0 ratio with respect to the magnet lift-off in the feasible design space is very small. Physically this might be explained with the high magnetic permeability of steel, which causes the magnetic flux lines to strongly alter their direction at the air to steel boundary (continuity of the normal component of the magnetic flux density and tangential component of the magnetising field at interfaces), which may be less susceptible to the lift-off distance than to the magnet diameter. Thus, from all the optimization runs that returned a better A0-S0 ratio than 75 dB, the one with the highest A0 amplitude in the far field is selected as the global optimum and is listed as the 'optimal design' in Table 2. Another observation that can be made from the optimisation is that the optimal magnet diameter is approximately half the wavelength of the A0 mode at the assumed operation point and for the given coil dimensions.

The optimal design, however, requires a magnet with a diameter that is not commercially available. For that reason, the magnet diameter is set to the closest commercially available one (diameter of 20 mm) and then the optimisation is rerun to determine a new magnet lift-off distance, approximately matching the performance of the optimal design. This design is termed 'proposed realisation' in Table 2 and is physically implemented for experimental validation of the FE model. Table 2 also lists the A0-S0 ratio for the same design parameters, when both the Lorentz and magnetisation force are considered. For the optimal design, the predicted A0-S0 ratio drops to around 27 dB and for the proposed realisation to 29 dB, when the magnetisation force is additionally considered.

Naturally, by looking at the performance drop due to including the magnetisation force into the model, the question arises, whether an optimisation with both excitation forces would lead to an even better design. For this, the A0-S0 ratio is calculated as a function of the magnet diameter for the lift-off of 2.1 mm (proposed realisation) under consideration of both excitation mechanisms. The influence of the lift-off is disregarded here with the argument above of only small changes to the magnetic flux lines due to the change in magnet lift-off. The result of this is illustrated in Figure 5, where it can be seen that for the case of only the Lorentz force excitation, there is a clear maximum at a magnet diameter of 20 mm, as expected. This behaviour is also observed in [29], where the A0-S0 ratio is studied as a function of the cone angle, which can be controlled via the magnet diameter. The excitation with both the Lorentz and magnetisation force does not exhibit a unique maximum A0-S0 ratio within the considered interval for the magnet diameter, but takes its largest value at a magnet diameter of 5 mm on the lower bound on the magnet diameter. There, the mode selectivity is significantly improved compared to that of a 20 mm magnet, however, due to the smaller magnet, the overall A0 mode sensitivity reduces significantly (approximately 18 dB when going from 20 mm to 5 mm magnet diameter),

since the reduced magnetic flux density within the skin depth layer reduces the magnitude of the exciting forces.

The evaluation of the feasible design space shows that in case of both excitation mechanisms, the performance indeed peaks at the lowest magnet diameter and lift-off and exhibits a smooth decrease in A0-S0 ratio with increasing magnet diameter and lift-off. In contrast, when only considering the Lorentz force, there is a region of high A0-S0 ratio for magnet diameters around 20 mm, which is fairly independent of the magnet lift-off. Outside this region of a high A0-S0 ratio, the A0-S0 ratio drops steeply as illustrated in Figure 5. The reason for there not being a clear maximum when both excitation forces are considered is traced back to the S0 amplitude, which is significantly higher (almost 100 times, see Figure 9 (bottom) at 50 kHz) in case of both excitation mechanisms, when compared to the case of only the Lorentz force, whereas the A0 amplitude remains almost unchanged in that comparison.

4.2 Experimental Validation of the Models

The finding from the previous section of a vast drop in A0-S0 ratio when considering the magnetisation force as an additional excitation mechanism requires an experimental validation of the FE model, in order to draw conclusions about the optimisation process and its feasibility for EMAT design. In the following, first the experimental setup is presented, followed by the validation of the Lorentz force model on an aluminium plate and the combination of the Lorentz and magnetisation force on a steel plate.

4.2.1 Experimental Setup

The EMAT prototype based on the proposed realisation is displayed in Figure 6 as it rests on a steel plate. The permanent magnet, which has been modelled with a height of 20 mm, consists

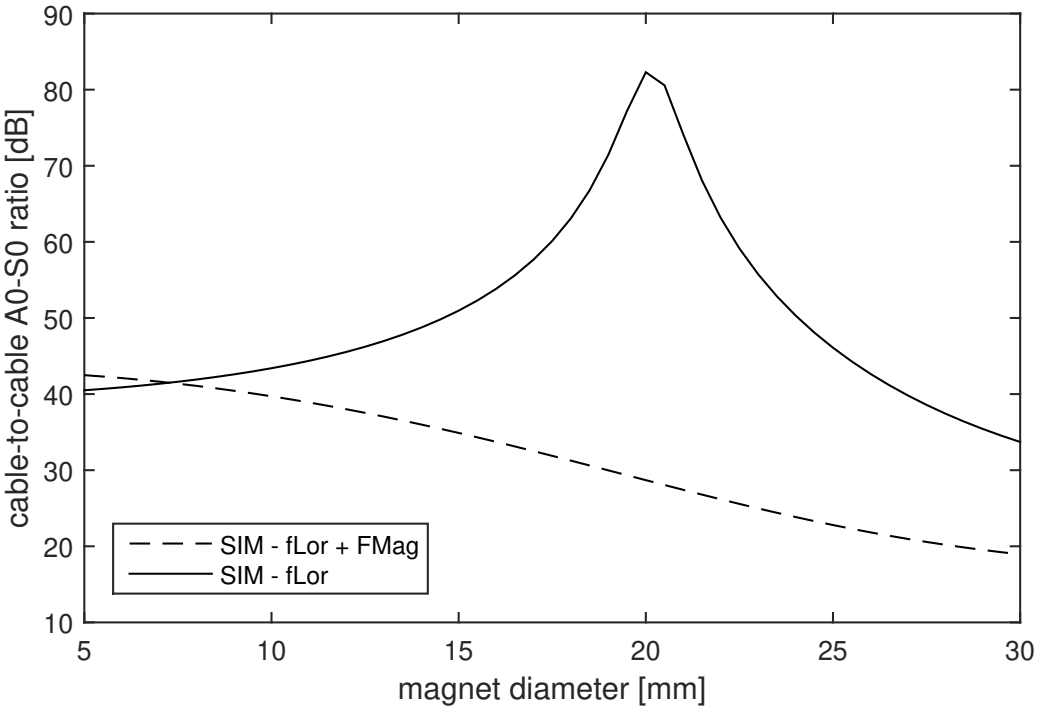

Figure 5: Cable-to-cable A0-S0 ratio as a function of the magnet diameter for the proposed realisation (magnet lift-off distance of 2.1 mm) on a steel plate and at 50 kHz (fd=0.5 MHz-mm). The curve with only the Lorentz force excitations matches with the findings from [29].

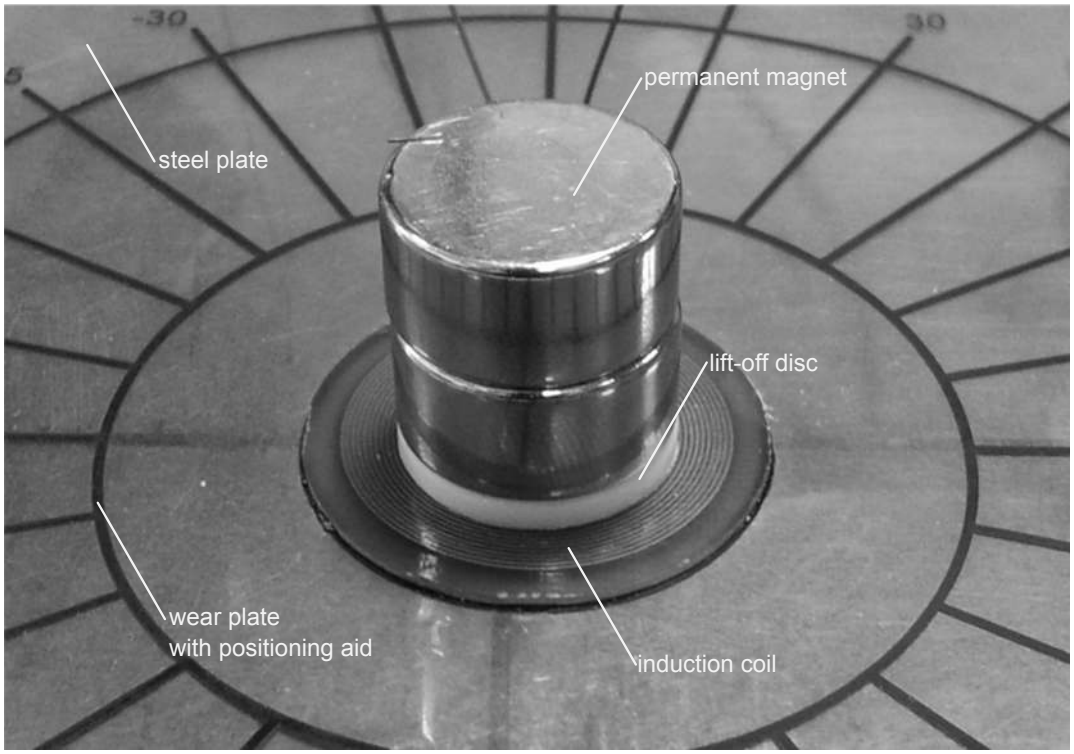

Figure 6: EMAT prototype for the proposed realisation in Table 2.

of two magnets (Magnet Expert Ltd., Tuxford, UK, part number F646) of 10 mm height that are stacked on top of each other. The magnet lift-off from the coil is established with a plastic disc that is filed down to 2.1 mm thickness to match the lift-off of the proposed realization. The coil is a two layered PCB coil that is taken from [11], where it is the coil of EMAT VII. A wear plate is placed under the coil, which serves the purpose of protecting the coil, while moving the EMAT along the steel plate. The wear plate is a simple plastic foil and the combined height of the wear plate and the coil is 0.9 mm, which corresponds to the value of the height of the coil in the FE model. Furthermore, the induction coil is glued to the wear plate to reduce the number of movable components in the prototype. This allows higher positioning accuracy for the permanent magnet with respect to the coaxial position relative to the induction coil. The two ports of the PCB induction coil are connected to a BNC connector for the connection with the measurement instrumentation.

The experimental setup is illustrated in Figure 7 for the measurements on a steel plate. Two identical EMAT prototypes are deployed on a 1.2 m by 1.2 m square steel plate with a thickness of 10 mm and are operated in pitch-catch mode. The separation distance is selected as 600 mm and both EMATs are placed at a distance of 300 mm from the plate centre on the symmetry line, as indicated in Figure 7. This separation distance of 600 mm is chosen as it allows good distinction between the first arrival S0 and A0 Lamb mode wave packets and their reflections from the plate edges. This is especially important for lower frequencies, as the group velocities are more different and the S0 edge reflection wave packets may superimpose on the A0 first arrivals, but it is ensured that the peaks of the S0 and A0 wave packet can still be separated from each other. A computer is used to control a Handyscope HS3 (TiePie Engineering, Sneek, The Netherlands) digital oscilloscope with integrated arbitrary function generator. The waveform generated with the Handyscope HS3 is amplified using a Hafler P1500 amplifier, prior to being fed into the sending EMAT. The receiving EMAT is connected to the Handyscope HS3 via a custom built EMAT receiver amplifier with a gain of approximately 95 dB.

The waveform transmitted by the sending EMAT is a five cycle Hann-windowed toneburst,

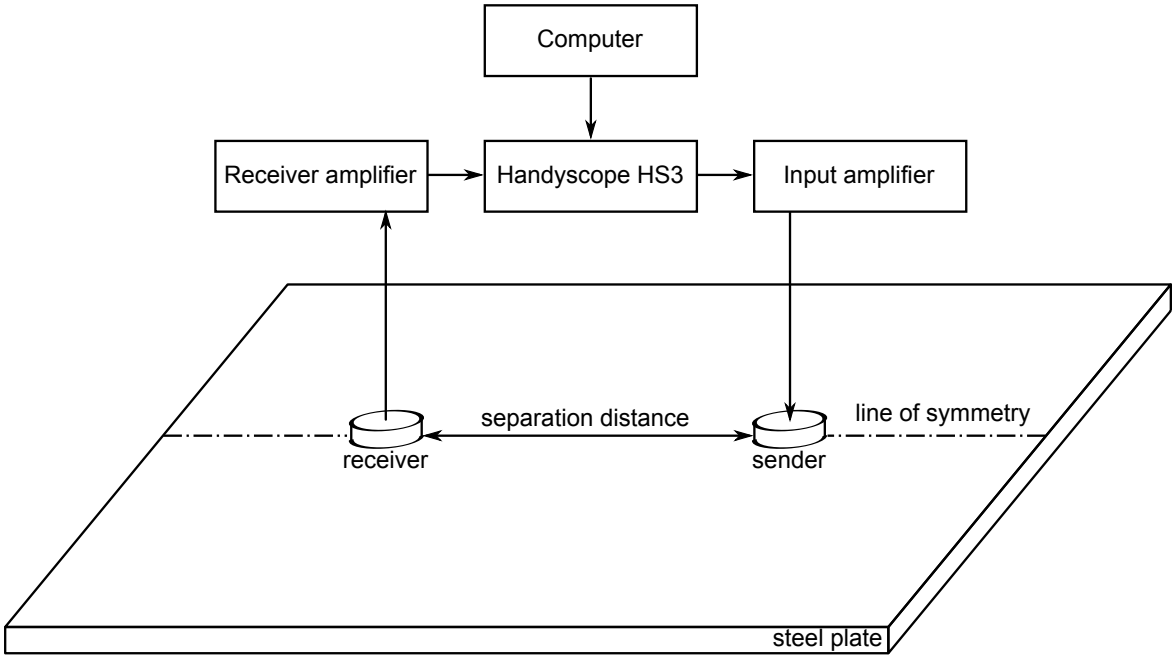

Figure 7: Experimental setup for the measurements on a plate, showing the instrumentation used.

following the FE simulations. The signal measured at the receiver is digitally filtered in addition to the hardware filtering of the EMAT receiver amplifier, limiting the bandwidth to the frequency band of interest. In the case of this paper, this means that the main lobe and the first side lobes of the amplitude spectrum of the input toneburst are considered, as discussed in the model overview section. The filtered voltage time traces are averaged 5000 times in order to reduce incoherent noise to a negligible level. This is particularly important for the S0 mode, whose amplitude may be very low. For verification purposes, the waveform sent to the sending EMAT is monitored for distortions by measuring the input current with a current transformer. The quantisation of the measured signals uses a 12 bit resolution for the amplitudes with a range of $200\,\mathrm{mV}_{p-p}$, which is the lowest range available with the Handyscope HS3 employed. The typical amplitude of the measured noise ranges at around $2\,\mathrm{mV}_{p-p}$ and has been determined based on the time traces for the higher centre frequencies, as the S0 mode can be clearly identified and therefore only experimental noise is present between the S0 wave packet and the cross-talk.

The validation of the FE model is conducted by considering the A0-S0 ratio as a function of the centre frequency. This approach also helps to eliminate any effect of the frequency response of the measurement electronics, as it is assumed that the frequency response of the measurement electronics is time-invariant and therefore affecting both the A0 and S0 mode equally when considering the same frequency range. Further, it is expected that the mode selectivity changes with the centre frequency, as the coil geometry is no longer matched well with the A0 wavelength and the excitation force direction no longer suppresses the S0 mode well. This is especially important, considering the fairly high A0-S0 ratio of the proposed realisation at the given operation point, as with a dropping A0-S0 ratio, the S0 amplitude may be more reliably determined. The behaviour of the A0-S0 ratio as a function of centre frequency also determines the frequency range of operation for the EMAT prototype for the required operation conditions. The centre frequency is varied from 40 kHz in steps of 5 kHz to

130 kHz. The A0 and S0 amplitudes are determined by the maximum of the wave envelope via the Hilbert transformation of the respective wave packets in the measured voltage-time traces. The Hilbert transformations of the wave packets are time-gated, according to the expected arrival times. The A0-S0 ratio is computed from the Lamb mode amplitudes using equation (7) assuming $\alpha = 1$ for simplicity and represents the cable-to-cable performance.

4.2.2 Test on Aluminium Plate

The experiments on an aluminium plate allow the validation of the FE model for the Lorentz force excitation mechanism, as aluminium exhibits only negligible paramagnetic properties. The comparison of the experimental measurements and the simulation are illustrated in Figure 8, where the A0-S0 ratio, as well as the normalised A0 and S0 amplitudes, are shown.

From Figure 8 (top), it can be seen that the A0-S0 ratio decreases with increasing centre frequency, for both simulation and two independent experiments. This is to be expected, as the average diameter of the coil is no longer well matched to half the wavelength, nor is the orientation of the body force matched to the mode shape of the A0 mode any longer. The comparison of simulation and experiment exhibits very good agreement for centre frequencies above 80 kHz. Above 80 kHz, the amplitudes of the A0 and S0 mode can be reliably determined from the measured voltage-time traces and therefore the A0-S0 ratio can be reliably computed. Below 80 kHz, the experimental A0-S0 ratio tends to plateau at around 35 dB to 40 dB, whereas the simulated A0-S0 ratio continues to rise. This behaviour of the experimental A0-S0 ratio can be explained with the experimental noise that superimposes the S0 amplitude and therefore masks it for very low S0 amplitudes.

Figure 8 also shows the A0 (middle) and S0 (bottom) amplitudes for both the simulation and two experimental datasets. Both the A0 and S0 amplitudes have been normalised with the maximum value of the A0 mode for the respective datasets, in order to facilitate an easier comparison. The maximum of the A0 amplitude is selected as the gauging condition, because it is least affected by experimental noise and therefore the most reliable quantity to consider. This can be argued by considering the relative variation between the two experimental datasets across the range of centre frequencies, also implying consistency of the measurements. The maximum A0 amplitude occurs at 40 kHz for both simulation and experiment and the normalised A0 amplitude drops with increasing centre frequency. This behaviour can be again explained with the argument above for the A0-S0 ratio. The experimental and simulated normalised A0 amplitudes show good agreement, especially for the higher frequencies, implying that the model approximates the A0 amplitude drop-off well. The normalised S0 amplitude increases slightly with increasing centre frequency for both simulation and experiment and the comparison between simulation and experiments exhibits a similar trend, however, the experimental S0 amplitudes are higher than the simulated ones. This may be due to the generally large A0-S0 ratio, as the S0 amplitude is very low (always below 3 mV and therefore barely above the experimental noise floor of around 1 mV) and therefore expected to be biased by the experimental noise.

In conclusion, it is found that the FE model matches the experimental data recorded on an aluminium plate well and is therefore a valid representation of the EMAT when the Lorentz force is the only excitation mechanism. Further, it is shown that the EMAT exhibits good A0 mode purity for centre frequencies of up to 70 kHz on a 10 mm thick aluminium plate.

4.2.3 Test on Steel Plate

Unlike the aluminium plate, the steel plate exhibits a high magnetic permeability and therefore this needs to be accounted for by the FE model. Additionally to the Lorentz force, now the magnetisation force needs to be considered, as well as the influence of the relative magnetic permeability on the Lorentz force. For this, the simulated performance of the EMAT for the case of only the Lorentz force and the case of both Lorentz and magnetisation force are compared to

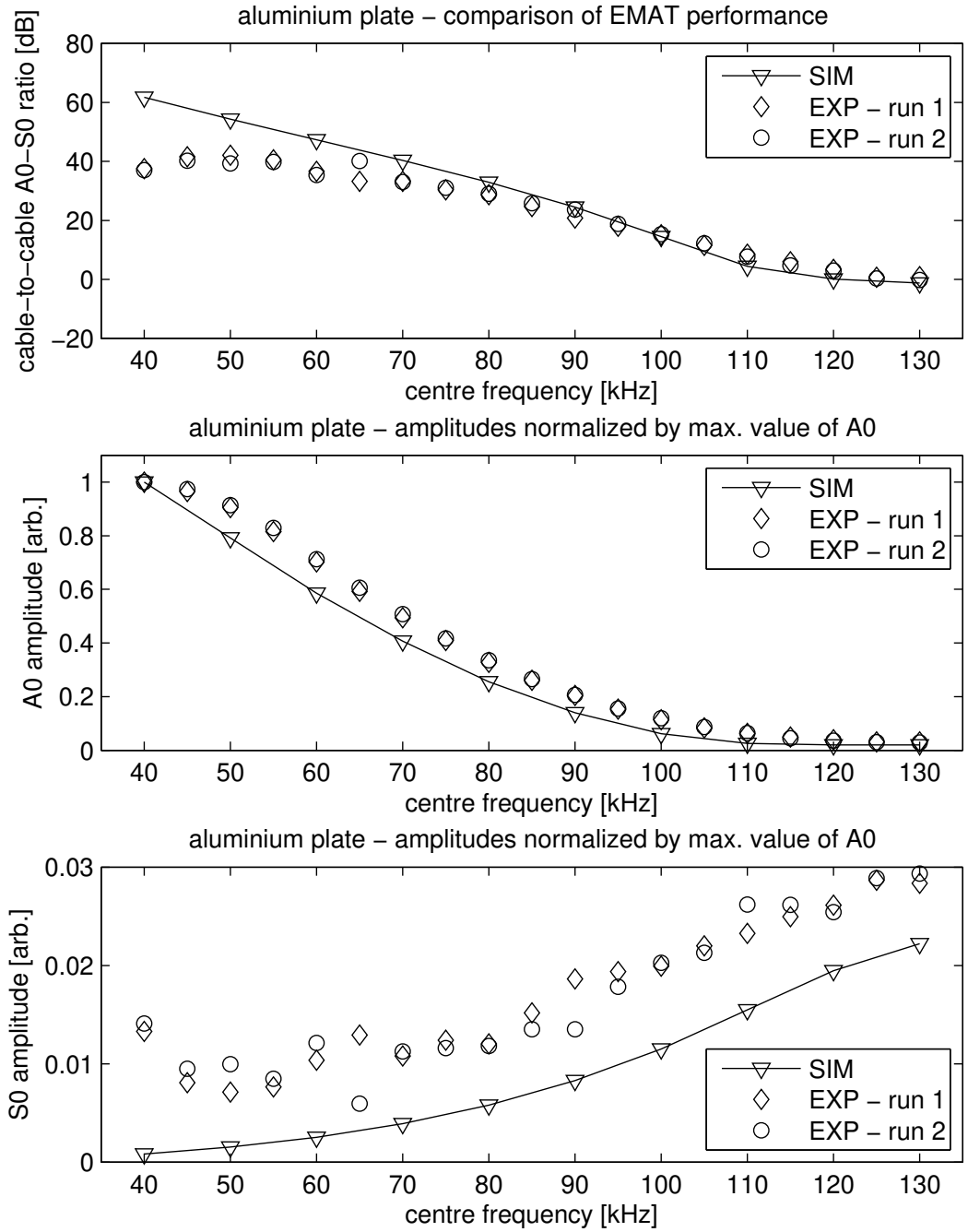

Figure 8: Comparison of cable-to-cable A0-S0 ratio (top), A0 amplitude (middle) and S0 amplitude (bottom) between the COMSOL simulation and two independent experimental measurements for an aluminium plate, showing good agreement and rendering the modelling of the Lorentz force valid. The A0 and S0 amplitudes are scaled by the maximum of the A0 amplitude.

the measured performance on a steel plate from eight measurements (the evaluation considers the experimental mean and standard derivation for representation only). The comparison is again achieved via the A0-S0 ratio as a function of the centre frequency.

In Figure 9 (top), the A0-S0 ratio is illustrated as a function of the centre frequency, where

it can be seen that for both experiment and simulation the A0-S0 ratio drops with frequency. The drop can be again explained with the same argument as in the aluminium plate case. From Figure 9 (top) it can also be seen that the case of only the Lorentz force as the excitation

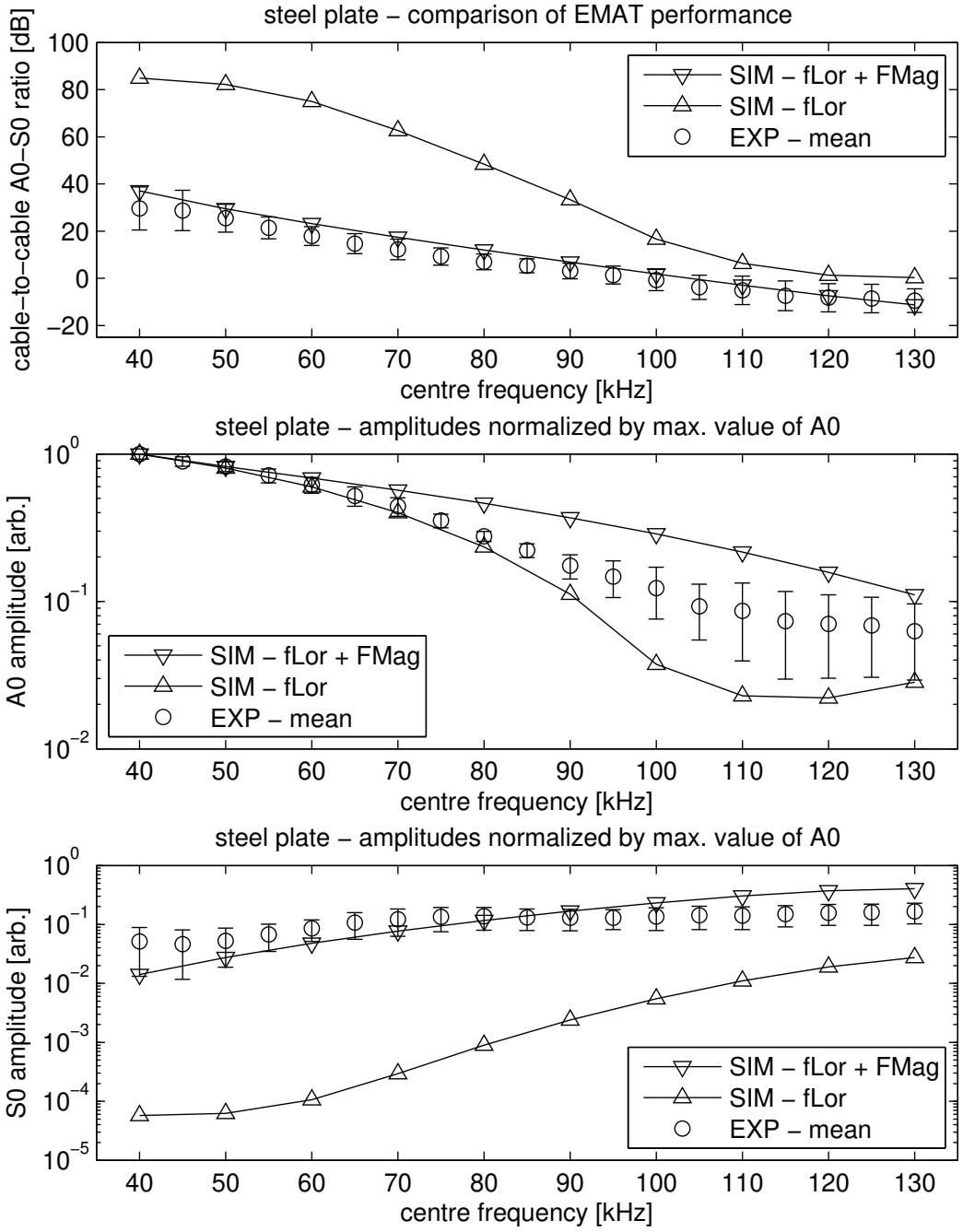

Figure 9: Comparison of cable-to-cable A0-S0 ratio (top), A0 amplitude (middle) and S0 amplitude (bottom) between the COMSOL simulation and experimental measurements for a steel plate, showing good agreement for the case where both excitation mechanisms are considered. The error bars indicate the standard deviation of the eight experimental measurements and the A0 and S0 amplitudes are scaled by the maximum of the A0 amplitude.

mechanism greatly overestimates the measured A0-S0 ratio, especially for lower frequency and the operation point. On the other hand, good agreement between simulation and experiment is found when the magnetisation force is considered on top of the Lorentz force as an excitation mechanism.

From the error bars of the experimental data it can be seen that for lower frequencies (<60 kHz) and higher frequencies (100 kHz<) there is an increased variation in the A0-S0 ratio, when compared to frequencies in the middle of the considered frequency range. One explanation for this is that for low frequencies the S0 amplitude and for high frequencies the A0 amplitude is affected by experimental noise, which can be seen from the variations of the measured A0 and S0 amplitudes in Figure 9 (middle) and (bottom) respectively. Also, the absolute amplitude values recorded for the respective modes at low and high frequencies (around 3 mV or less) are found to be on the order of the noise amplitudes of approximately 1 mV. For frequencies between 60 kHz and 100 kHz the A0 and S0 amplitudes can be reliably determined from the measured time traces, which leads to the small variations in the A0-S0 ratio.

In Figure 9 (middle), the normalised A0 amplitudes are compared and the same normalisation as in the aluminium plate case is used. From Figure 9 (middle) it can be seen that the A0 amplitude decreases with increasing centre frequency for both simulation and experiment. When comparing the experimental A0 amplitudes with those from both simulations, agreement with both simulations is found. Below centre frequencies of 90 kHz, the A0 amplitude is mostly explained with the Lorentz force excitation only. Above 90 kHz, the experimental A0 amplitude starts to vary strongly and takes values between the two curves of the simulated A0 data. Moving on to the normalised S0 amplitudes, Figure 9 (bottom), good agreement between the experimental measurements and the case where both Lorentz and magnetisation force are considered is found. From this it can be concluded that the decrease in A0-S0 ratio, when additionally considering the magnetisation force, may be explained by the increase in S0 amplitude rather than the decrease in A0 amplitude.

As a conclusion from the comparison of the experiment on a steel plate with the FE model, good agreement is found when the Lorentz and magnetisation force are considered by the model, rending the model valid. The discrepancy between the model and simulation could be traced back to the experimental limitations of low signal amplitudes and a low signal-to-noise ratio, however, these may not be the only limitations. The remaining discrepancy may be attributed to the incomplete ferromagnetic material model in conjunction with magnetostriction, as this is not accounted for by the model due to the vast uncertainties in the material parameters. For a normal bias magnetic field shear wave EMAT, the amplitude caused by magnetostriction may be up to 30% of the amplitude of the Lorentz force, as discussed in [26]. Also the effect of magnetostriction may not be equal for the A0 and S0 mode due to the direction of interaction, explaining some of the discrepancy in terms the A0-S0 ratio. If the assumption is made that for the EMAT design considered in this experimental study with a less normal bias magnetic field, behaves similarly to the findings in [26], but less strongly pronounced, this could explain the remaining discrepancy between the simulation and experiment. From this it is also clear that this is one of the limitations of the finite element model, however, the predictions are still sufficiently accurate for the purpose of the model. Further, it is found that the EMAT exhibits an A0-S0 ratio that matches the requirements for A0 tomography of approximately 30 dB S0 suppression.

4.3 Numerical Robustness Study

There are a number of uncertainties associated with the EMAT, which will be present when it is manufactured and used. To study the effect of typical parameter variations on the transducer performance, a numerical robustness study is conducted, using both the Lorentz and magnetisation force as excitation mechanisms. The goal is to evaluate whether the performance of the proposed realization breaks down for small variations of the design. The two aspects regarded

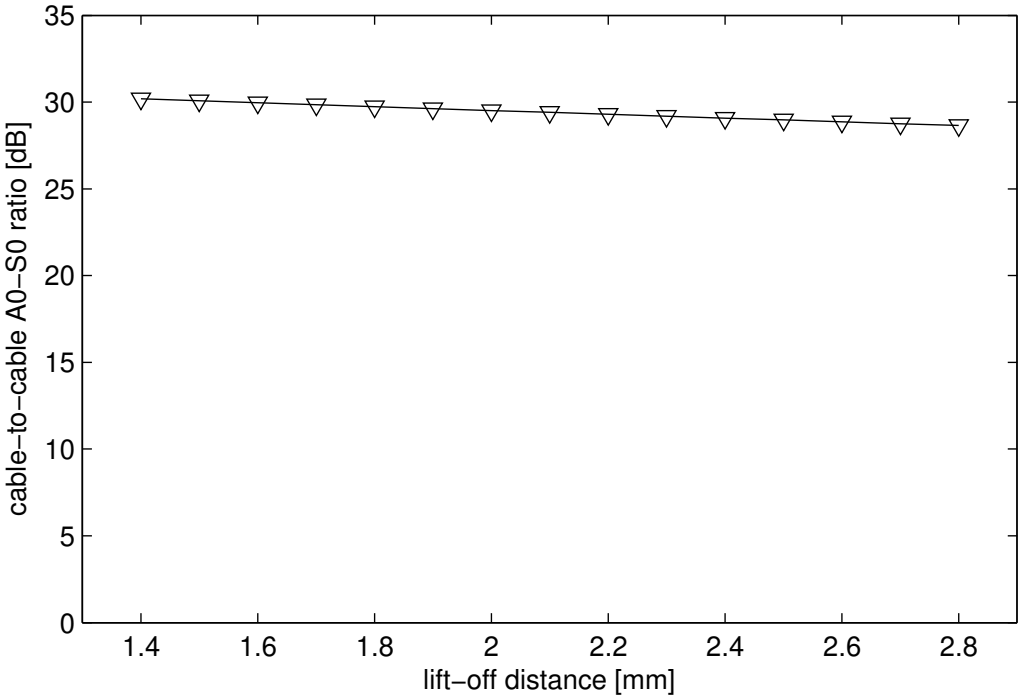

Figure 10: Simulated A0-S0 ratio as a function of the magnet lift-off for the proposed realisation. The triangles denote the evaluation points for the lift-off.

in this study are the magnet lift-off and the uncertainty in the magnetic permeability.

4.3.1 Magnet Lift-off

The sensitivity of the EMAT to magnet lift-off is of importance for the practical realization, as it determines the necessary precision for the manufacturing of the EMAT. For this study, the lift-off distance is varied from 1.4 mm to 2.8 mm and the cable-to-cable A0-S0 ratio is illustrated as a function of this parameter in Figure 10. The triangles in Figure 10 denote the evaluation points for the lift-off and it can be seen that the A0-S0 ratio does not change significantly within the regarded interval. The A0-S0 ratio remains above 25 dB for the entire interval and decreases slightly with increasing lift-off distance. This is an expected result, as with increasing magnet lift-off distance the direction of the magnetic flux lines in the skin depth layer are slightly changed and therefore slight changes in the mode selectivity are expected. It needs to be noted that for an increase in lift-off distance, the magnetic flux density decreases and therefore the A0 mode sensitivity may decrease. For very small lift-off distances, eddy currents may form in the magnet that may negatively influence the sensitivity. Further, as discussed earlier, the magnet lift-off is not the dominant parameter in the optimization, which is shown by the only small change in performance over the interval of lift-off distances. These results imply robustness of the proposed realization of the EMAT design to a variation in lift-off distance. Therefore, the tolerances on the magnet lift-off for manufacturing can be relaxed.

4.3.2 Magnetic Permeability

There is a significant level of uncertainty in the relative magnetic permeability of the steel plate, as this may for example be influenced by the composition of the steel and the magnetization history of the material, additionally to the paramagnetic approximation of the ferromagnetic material. Therefore the influence of the magnetic permeability on the A0-S0 ratio is studied

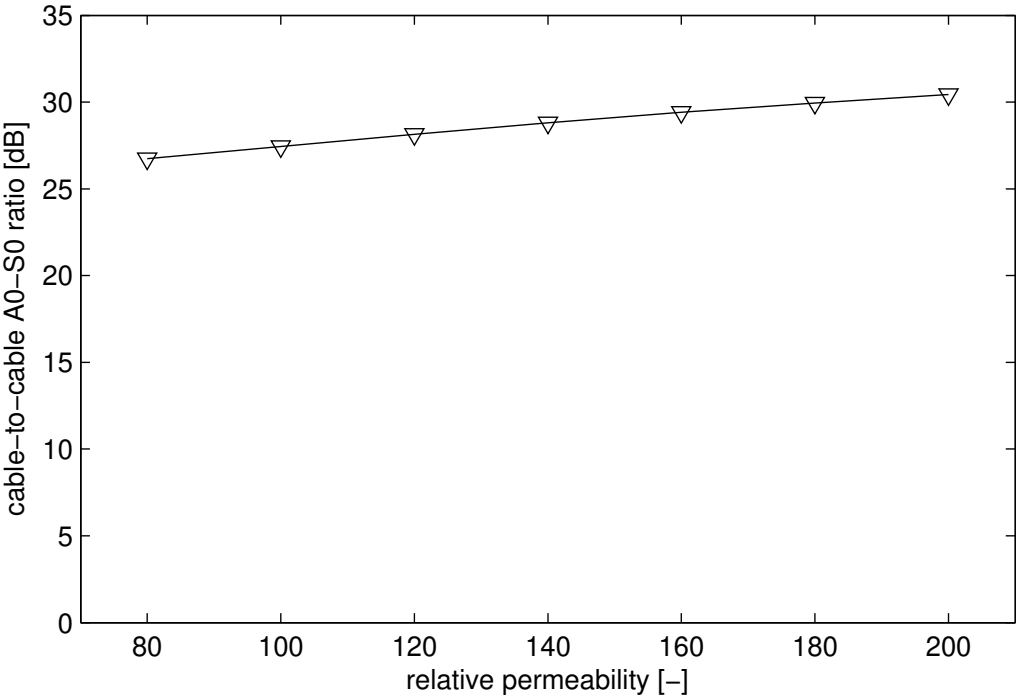

Figure 11: Simulated A0-S0-ratio as a function of the relative permeability of steel for the proposed realisation. The triangles denote the evaluation points for the various relative magnetic permeabilities.

within a range of 80 to 200 for the relative magnetic permeability, which is typical for steel [22]. In Figure 11, the cable-to-cable A0-S0 ratio is depicted as a function of the relative magnetic permeability within the aforementioned range. It can be seen that the A0-S0 ratio does not vary significantly within this range implying that the relative permeability exhibits negligible influence on the Lorentz and magnetization force excitation mechanism. This behaviour can be explained by the skin depth (equation (1)), which varies only slightly due to the change in the relative permeability, therefore only slightly modifying the region where significant Lorentz and magnetization forces are acting. Also, the skin depth is always much smaller than the acoustic wavelength ($\delta \ll \lambda$) for all values of relative magnetic permeability considered here, which suggest that only a negligible influence is to be expected. In conclusion, the influence of the magnetic permeability on the EMAT performance is found to be small for typical variations, implying robustness.

4.4 Model-based Design Approach

Having validated the FE model on an aluminium and a steel plate, the EMAT design strategy needs to be revisited. Based on the findings in the previous sections, the drop in A0-S0 ratio in case of the steel plate may be explained with an increase in the S0 amplitude rather than a decrease in A0 amplitude when additionally considering the magnetisation force in the model. Also, in Figure 5 it can be observed that when including both excitation forces, there is no clear maximum within the feasible range of magnet diameters, but the maximum occurs at the lower bound of the interval. Using an optimisation scheme to find the maximum A0-S0 ratio therefore converges to the minimum magnet diameter, which improves the mode selectivity, however, the mode sensitivity is greatly reduced, due to the reduced magnet size and subsequent reduction in excitation force amplitude. For a successful EMAT design, the duality of mode selectivity and sensitivity needs to be considered and this is clearly not the case when including the

magnetisation force into the optimisation procedure, as the performance criterion only considers the selectivity.

A model-based design approach is therefore proposed whereby in a first step, only the Lorentz force is considered in the model and an optimisation is run to find the maximum A0-S0 ratio, as the magnetisation force is difficult to model. Since this represents a severe overestimation of the transducer performance, in a second step the magnetisation force is included in the model to calculate a more realistic estimation of the transducer performance for the previously optimised design, using the finding that the magnetisation force mostly affects the S0 amplitude.

The major disadvantage of this approach is that the optimisation must not yield the best possible A0-S0 ratio, as for example for a slightly smaller magnet diameter, the selectivity might be better, whereas the sensitivity might be only slightly influenced. An example of this is the comparison of a magnet of 15 mm diameter and of 20 mm diameter. From Figure 5 and for the case of both excitation mechanisms, it can be seen that there is an increase of around 6 dB in mode selectivity when going to the smaller magnet diameter. In parallel, the sensitivity only drops by 3 dB when considering the smaller magnet diameter, rendering the 15 mm magnet diameter design better, due to the small drop in sensitivity. However, since there is no easy way of arriving at the 15 mm magnet diameter design based on the optimisation, using the two step approach is the best modelling approach to determine an improved EMAT design, at the cost of sacrificing some selectivity and given the underlying uncertainty in accurately estimating the magnetic permeability.

In case of non-magnetic materials such as aluminium, this approach using the optimisation to find the peak performance (the magnetisation force re-evaluation step is omitted) will lead to the best possible compromise between selectivity and sensitivity, as there is a clear and unique maximum for the A0-S0 ratio, as shown in [29] and found here. Alternatively, a different performance criterion could be developed that considers both the mode selectivity and sensitivity simultaneously, for example by finding the maximum of the product of the A0-S0 ratio and the greater of the A0 and S0 amplitude values.

As a concluding remark, the optimisation only looks at the magnet diameter and magnet lift-off as parameters, however, the model-based design approach is not limited to that. The optimisation may use other parameters, which are capable of shaping the magnetic flux, as this is the underlying physics which is to be used for optimisation. One example of this is for example given in the patent in [32], where an optimised and an unoptimised design are compared, clearly showing that this is a feasible approach. Similarly, EMAT VII of [11] was available to the authors and uses the same coil as in the EMAT design here, but with a magnet of diameter 32 mm. In an experimental comparison, it is found that there is a clear improvement in terms of the A0-S0 ratio, for the EMAT with a magnet diameter of 20 mm, clearly showing the feasibility of the presented model-based design. The measured performance at 50 kHz also matches that presented in Figure 9(c) of [11].

5 Summary

An omni-directional low frequency A0 Lamb wave EMAT operating on a steel plate has been developed with a target A0-S0 ratio of approximately 30 dB. In a first step, a parametric FE model of the design concept has been implemented in COMSOL, where the bias magnetic field is calculated initially, then combined with the eddy current caused by the induction coil to produce a force. In a second step, a numerical optimization process employing a genetic algorithm has been set up and the EMAT design is optimized to yield an improved A0 mode selectivity. The parameters subjected to optimization are the magnet diameter and the magnet lift-off, which control the direction and magnitude of the exciting forces in the skin depth layer and therefore the mode selectivity.

For the initial optimisation process, only the Lorentz force is considered for the wave exci-

tation besides the magnetisation force and from the optimised design a physical prototype has been built. The FE model is validated for measurements on an Aluminium plate for the Lorentz force excitation mechanism and on a steel plate for both the Lorentz and magnetisation force. For the steel plate, it is found that only considering the Lorentz force leads to a significant overestimation of the mode selectivity, as the S0 amplitude is underestimated by the Lorentz force, but the A0 amplitude remains mainly uninfluenced. Further, it has been found that additionally including the magnetisation force into the optimisation process leads to a better mode selectivity, however, the optimisation drives the optimum to the minimum magnet diameter and therefore reduces the sensitivity. A numerical robustness study is conducted and robustness is found for fairly large variations of the magnet lift-off and the magnetic permeability. Based on these findings, a two-step model-based design approach is proposed whereby in the first step, the Lorentz force is used for excitation and an optimised design is found. In the second step, a realistic estimate of the mode selectivity of the optimised design is obtained by additionally considering the magnetisation force.

Acknowledgements

The authors would like to acknowledge funding from the Engineering and Physical Science Research Council (EPSRC) grant number EP/H040072/1 and the industrial sponsors Shell and Petrobras.

Compliance with Ethical Standards

The authors are unaware of any potential conflicts of interest. No human participants or animals were harmed in the course of the underlying research.

References

[1] J. Hou, K. R. Leonard, and M. K. Hinders, "Automatic multi-mode Lamb wave arrival time extraction for improved tomographic reconstruction," *Inverse Problems*, vol. 20, no. 6, pp. 1873–1888, 2004.

[2] C. A. Miller and M. K. Hinders, "Classification of flaw severity using pattern recognition for guided wave-based structural health monitoring," *Ultrasonics*, vol. 54, no. 1, pp. 247–258, 2014.

[3] A. Volker and H. Vos, "Experimental results of guided wave travel time tomography," *Review of Progress in QNDE, edited by D. O. Thompson and D. E. Chimenti, AIP Conference Proceedings*, vol. 1430, no. 1, pp. 1968–1975, 2012.

[4] A. Volker and R. Vos, "Annular plate inspection using guided wave tomography," *Review of Progress in QNDE, edited by D. O. Thompson and D. E. Chimenti, AIP Conference Proceedings*, vol. 1511, pp. 745–752, 2013.

[5] A. Volker and T. van Zon, "Guided wave travel time tomography for bends," *Review of Progress in QNDE, edited by D. O. Thompson and D. E. Chimenti, AIP Conference Proceedings*, vol. 1511, pp. 737–744, 2013.

[6] P. Huthwaite and F. Simonetti, "High-resolution guided wave tomography," *Wave Motion*, vol. 50, no. 5, pp. 979–993, 2013.

[7] P. Huthwaite, "Evaluation of inversion approaches for guided wave thickness mapping," *Proceedings of the Royal Society A: Mathematical, Physical and Engineering Sciences*, vol. 470, no. 2166, 2014.

[8] P. Huthwaite, R. Ribichini, P. Cawley, and M. J. S. Lowe, "Mode selection for corrosion detection in pipes and vessels via guided wave tomography," *IEEE Transactions on Ultrasonics, Ferroelectrics and Frequency Control*, vol. 60, pp. 1165–1177, 2013.

[9] P. Belanger, P. Cawley, and F. Simonetti, "Guided wave diffraction tomography within the Born approximation," *IEEE Transactions on Ultrasonics Ferroelectrics and Frequency Control*, vol. 57, pp. 1405–1418, 2010.

[10] M. Hirao and H. Ogi, *EMATs for Science and Industry: Noncontacting Ultrasonic Measurements*. Kluwer Academic Publishers, 2003.

[11] P. D. Wilcox, M. J. S. Lowe, and P. Cawley, "The excitation and detection of Lamb waves with planar coil electromagnetic acoustic transducers," *IEEE Transactions on Ultrasonics, Ferroelectrics and Frequency Control*, vol. 52, pp. 2370–2383, 2005.

[12] R. H. Koch, A. May, and J. Li, "Electromagnetic acoustic transducers for use in ultrasound inspection systems." US Patent 7,426,867, 2008.

[13] M. Lowe and B. Pavlakovic, "DISPERSE user manual." http://www3.imperial.ac.uk/nde/products%20and%20services/disperse, 2013.

[14] F. C. Moon, *Magneto-solid Mechanics*. John Wiley & Sons Inc, 1984.

[15] D. Jiles, *Introduction to Magnetism and Magnetic Materials*. Chapman and Hall, 1998.

[16] J. Jackson, *Classical Electrodynamics Third Edition*. Wiley, Aug. 1998.

[17] M. Bellac and J. M. Levy-Leblond, "Galilean electromagnetism," *Il Nuovo Cimento*, vol. 14, pp. 217–234, 1973.

[18] C. T. Chian and F. C. Moon, "Magnetically induced cylindrical stress waves in a thermoelastic conductor," *International Journal of Solids and Structures*, vol. 17, pp. 1021–1035, 1981.

[19] R. B. Thompson, "A model for the electromagnetic generation of ultrasonic guided waves in ferromagnetic metal polycrystals," *IEEE Transactions on Sonics and Ultrasonics*, vol. 25, pp. 7–15, 1978.

[20] W. F. Brown, "Magnetic energy formulas and their relation to magnetization theory," *Rev. Mod. Phys.*, vol. 25, pp. 131–135, Jan. 1953.

[21] W. F. Brown, *Magnetoelastic Interactions*. Springer, 1966.

[22] R. Ribichini, P. B. Nagy, and H. Ogi, "The impact of magnetostriction on the transduction of normal bias field EMATs," *NDT & E International*, vol. 51, pp. 8–15, 2012.

[23] L. E. Malvern, *Introduction to the Mechanics of a Continuous Medium*. Prentice-Hall, 1969.

[24] J. D. Achenbach and Y. Xu, "Wave motion in an isotropic elastic layer generated by a time-harmonic point load of arbitrary direction," *The Journal of the Acoustical Society of America*, vol. 106, pp. 83–90, 1999.

[25] COMSOL Inc., "Documentation of COMSOL 4.3a." http://www.comsol.com/, May 2012.

[26] R. Ribichini, *Modeling of electromagnetic acoustic transducers*. PhD thesis, Imperial College London, 2011.

[27] Arnold Magnetic Technologies Corporation, "Datasheet of N42 Nd-Fe-B Magnets," 2009.

[28] M. V. K. Chari and P. Reece, "Magnetic field distribution in solid metallic Structures in the vicinity of current carrying conductors, and associated Eddy-current losses," *IEEE Transactions on Power Apparatus and Systems*, vol. 93, pp. 45–56, 1974.

[29] P. B. Nagy, F. Simonetti, and G. Instanes, "Corrosion and erosion monitoring in plates and pipes using constant group velocity Lamb wave inspection," *Ultrasonics*, vol. 54, no. 7, pp. 1832 – 1841, 2014.

[30] G. Winter, *Genetic Algorithms in Engineering and Computer Science*. Wiley, 1995.

[31] The MathWorks Inc., "Documentation of Matlab R2012b." http://www.mathworks.co.uk/, 2012.

[32] G. Instanes, P. B. Nagy, F. Simonetti, and C. L. Willey, "Measuring wall thickness loss for a structure," *Patent*, no. US20140208852 A1, 2014.